Journal of Energy Storage 154 (2026) 121124

Contents lists available at ScienceDirect

Journal of Energy Storage

journal homepage: www.elsevier.com/locate/est

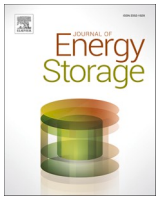

Research papers

Comparative in-operando analysis of lithium-ion cell swelling in pouch cells: Constant force versus foam-buffered quasi-constant force

Magdalena Karolina Zywolko [a], Andrew Paolo Cádiz [a], Felix Brauchle [a], Sascha Berg [b,c], Egbert Figgemeier [b,c,d,e,*]

[a] Mercedes-Benz AG, Mercedesstraße 130/6, 70327, Stuttgart, Germany
[b] Center for Ageing, Reliability and Lifetime Prediction of Electrochemical and Power Electronic Systems (CARL), RWTH Aachen University, Germany
[c] Helmholtz Institute Münster (HIMS), IMD-4, Forschungszentrum, 52425, Jülich, Germany
[d] Juelich Aachen Research Alliance, JARA-Energy, 52425, Jülich, Germany
[e] Chair for Aging and Lifetime Prediction of Batteries, Institute for Power Electronics and Electrical Drives (ISEA), RWTH Aachen University, Campus Boulevard 89, 52074, Aachen, Germany

ARTICLE INFO

Keywords:
Eddy-current sensors
Pneumatic press
Compression
Swelling
Non-destructive
Lithium-ion batteries
Pouch cells

ABSTRACT

Accurate monitoring of thickness changes in lithium-ion batteries during operation is critical for understanding swelling behavior and its impact on performance and longevity. With the increasing focus on high energy density materials such as silicon-rich anodes, early-stage evaluation of cell swelling has become particularly important. In this study, we present a comparative analysis of two in-operando swelling measurement setups for small format pouch cells: (1) state-of-the-art pneumatic cell presses operating under constant-force conditions, and (2) a printed circuit board (PCB)-based eddy-current displacement sensors applying a quasi-constant preload force via compression pads. While pneumatic presses can be employed for in-operando swelling measurements under variable force, their size, cost, and complexity limit their widespread adoption. The PCB-based setup provides a compact, cost-effective alternative that enables long-term, high-resolution thickness measurements without the need for bulky equipment. Building on earlier work, we optimized the latter setup for long-term cycling with an emphasis on understanding the relaxation behavior of the compression pads and how it affects the thickness change measurements. Beyond serving as a mechanical fixture, the compression pad was found to beneficially influence electrochemical performance, highlighting its dual role as a functional component in cell testing. The results validate the PCB-based setup as a practical substitute for pneumatic presses and emphasize the performance advantages of incorporating a compression pad in in-operando measurements.

1. Introduction

The rapid electrification across industries, particularly in the automotive sector, has intensified the demand for high-performance and cost-competitive lithium-ion batteries (LIBs) [1]. According to recent studies, the electric vehicle (EV) market is expanding substantially, leading to a corresponding rise in battery demand and recycling infrastructure. This global transition toward electric mobility places additional emphasis on the optimization of battery systems [2,3]. A key challenge lies in achieving higher energy density to extend the driving range while minimizing the volume and weight of the battery pack and reducing its overall costs [1,4].

Key battery performance indicators (KPIs) in early-stage material development traditionally include gravimetric and volumetric energy density, cycle life, capacity retention, and cost per kWh [1]. While mechanical aspects like cell swelling during formation and cycling are well recognized, they are often secondary to electrochemical KPIs in the initial phase of material research. Although swelling may not immediately limit performance in small lab-scale prototypes, it plays a critical role in evaluating material suitability and predicting behavior in scaled-up formats and later, in modules and packs [5–8].

As research advances toward higher energy density electrode materials, the adoption of silicon and its derivatives in anode formulations has brought swelling to the forefront of materials research [1,9].

* Corresponding author at: Center for Ageing, Reliability and Lifetime Prediction of Electrochemical and Power Electronic Systems (CARL), RWTH Aachen University, Germany.
E-mail address: e.figgemeier@fz-juelich.de (E. Figgemeier).

https://doi.org/10.1016/j.est.2026.121124
Received 8 September 2025; Received in revised form 30 January 2026; Accepted 15 February 2026
Available online 23 February 2026

Increased silicon content leads to practical issues such as high-volume expansion at the particle level (up to 300%), which has a substantial impact on the cyclic aging performance [10,11]. Although silicon offers a high theoretical capacity (~3579 mAh g^{-1} at room temperature), it leads to mechanical degradation and capacity fade of the anode and consequently of the full cell [12,13]. One of the main aging mechanisms of such electrodes is contact loss from particle pulverization or even delamination of the entire electrode [14]. As a compromise, commercial cells often incorporate low amounts of silicon/carbon (Si/C) secondary particle composites or silicon oxide (SiOx) mixed in with graphite (Gr) to form anode blends (silicon contents of $\sim <$ 10 wt%), improving the energy density while limiting electrode expansion [4,15,16].

When characterizing swelling behavior, it is essential to distinguish between reversible thickness changes (due to lithiation and delithiation), often regarded as "breathing", and irreversible thickness growth caused by various cell degradation mechanisms [4,15]. The latter is often linked to the evolution of the state of health (SoH) and is induced by SEI layer growth, lithium plating, and gas generation [17]. During the initial formation phase, irreversible swelling dominates due to initial SEI formation as well as electrode relaxation or particle rearrangement. During subsequent cycling, irreversible swelling propagates at a much lower rate [4].

Previous studies have shown that applying external mechanical pressure to the cell stack can effectively suppress the negative effects of expansion during operation, as it ensures electrical contact between particles, prevents electrode delamination, and expels gas from between the electrode layers [4,10,18,19]. The mechanical requirements associated with applying this pressure depend on the cell format and therefore directly impact module and pack design [20]. In this context, two main modes of pressure application are typically distinguished: constant force and constant stiffness, often referred to as flexible and rigid compression, respectively [10,18]. At the cell level, flexible compression allows limited expansion while maintaining a relatively constant pressure [10,15], whereas rigid compression restricts dimensional changes and leads to internal pressure build-up [4,19].

In practical battery modules, pouch or prismatic cell formats are stacked and mechanically constrained to a fixed dimension, typically defined by the available installation space, before the structure is locked in place by a mechanical compression system [8,21]. This process imposes an initial preload pressure on the cells, which additionally experiences the module stiffness over cycle life. The battery module housing is required to endure both external mechanical loads (e.g., shock and vibration) and internal loads arising from cell behavior (e.g., breathing and irreversible swelling) [22]. In contrast, cylindrical cells are inherently mechanically constrained by their rigid metallic casing and therefore do not rely on external compression systems to maintain structural integrity [23–25]. Nevertheless, cylindrical cells also exhibit reversible breathing and irreversible internal pressure build-up during cycling. Managing this pressure evolution, along with associated dimensional changes (e.g., radial or axial expansion), remains a key challenge for long-term cell and module design [26].

One approach to accommodate cell expansion while maintaining mechanical constraint is the integration of compressible buffering elements, such as gap or compression pads, as interlayers between cells, enabling controlled expansion under a defined pressure over extended aging periods [6,27]. Moreover, these elements not only reduce the risk of direct contact between the module and the casing, thereby increasing overall safety, but also promote more homogeneous pressure distribution. In a study by Wünsch et al., it was shown that graphite/NMC 622 cells cycled with the buffering elements exhibited lower capacity loss [28]. Although compression pads can maintain pressure, they are electrochemically inactive and therefore reduce the energy density at the battery module level [27]. In addition, they also lead to pressure relaxation, as they are progressively compressed by swelling cells, deviating from ideal constant-force conditions. Although highly relevant, many existing investigations still rely on constant-force setups employing rigid pressing plates, which do not reflect the evolving mechanical boundary conditions in practical battery modules.

Some of the previously published constant-force setups include pneumatic [4,8] or electromechanical [29] presses, which enable very accurate and controlled force application, yet they are bulky and expensive limiting the materials screening activities. Many utilize a fixture of bottom and top plates where the pressure on the cell is maintained with springs attached at the corners of the top plate [22,28]. In a study by Müller et al., a three-plate setup with springs is proposed, where the top and bottom plates are fixed in place while the middle plate is moving [10]. Although these setups are much more compact, they are not as operationally advanced as the pneumatic presses [10]. Other approaches employ pressure-monitoring or dilatometer cells, which are constrained with a defined force but are typically limited to coin cell formats [30,31].

While Brauchle et al. (2023, 2024) [32,33] demonstrated that eddy-current-based setups with compression pads enable high-resolution, space-efficient, and cost-effective thickness measurements, the present work extends their approach to a direct comparison of two distinct in-operando swelling measurement systems. This study evaluates not only the applicability of these systems to long-term cycling but also their reliability under realistic mechanical constraints for silicon-containing lithium-ion cells. Specifically, we compare:

1) A state-of-the-art pneumatic cell press operating under constant-force conditions, equipped with three displacement sensors.
2) A PCB-based setup combining a quasi-constant preload force via compression foam under constant-gap constraints with four displacement sensors.

Earlier work validated these systems' ability to spatially resolve aging phenomena such as lithium plating and SEI inhomogeneity [33]. While sensor operation has been described in detail previously, these studies did not address the long-term mechanical relaxation of the foam under compression, nor did they provide a method to extract accurate cell swelling values from the experimental data. Furthermore, the investigated cells were large-format 45 Ah pouch cells, and the measurement concept has not previously been compared to state-of-the art swelling setups, such as a pneumatic press.

In this study, we provide comprehensive validation to determine whether the simpler, more compact, and cost-effective PCB-based setups can produce results comparable to those of high-precision pneumatic presses, with the aim of enabling their integration into high-throughput materials screening. Although single-layer pouch cells are used due to geometric compatibility with the PCB setup, application to larger formats remains possible for future investigations. Particular attention is given to non-trivial factors such as foam relaxation and fitting procedures at different pressures, which are critical for isolating cell swelling and ensuring reproducible results. Variability arising from foam morphology is quantified via standard deviations, and finally, the influence of buffered surfaces is evaluated with respect to improvements in electrochemical performance.

Together, these investigations present a framework for evaluating the performance and reliability of in-operando swelling measurement systems under realistic mechanical conditions. The study highlights both the mechanical characterization of compression pads and the methodological procedures required to obtain reproducible swelling data. This approach enables a direct comparison of single unit stack swelling results between compact PCB-based setups and actively controlled pneumatic presses, demonstrating the potential of the former for practical applications in battery screening and testing.

2. Experimental

Two distinct in-operando swelling measurement strategies were employed and compared:

- a constant-force configuration using pneumatic presses with hard/stiff endplates (unbuffered), and
- a quasi-constant force configuration using PCB-based setups with compression pads (buffered).

In parallel, control experiments were conducted in mechanical jigs without thickness monitoring to assess the influence of stiff endplates and endplates with compression pads (also referred to as "foams" or "buffering elements") on overall cell performance. The mechanical designs of all test benches are shown in Fig. 1 **(a)-(d)**.

2.1. Investigated cells

This study focused on two in-house assembled pouch cell formats:

- **Type 1**: single-layer sandwich cells (~180 mAh), and
- **Type 2**: double-layer cells (~3.2 Ah).

Type 1 cells consisted of two single-side coated anodes (SSA) and one double-side coated cathode (DSC) in between, separated by two 16 µm polypropylene separator (HiporeTM, Asahi Kasei) forming a total of two unit stacks. Type 2 cells, in contrast, comprised six double-side coated anodes (DSA) and five DSCs, stacked alternately with the same separator material between each layer, resulting in ten unit stacks. Cells were filled with 5 mL/Ah for Type 1 and 2.5 mL/Ah of electrolyte for Type 2 and evacuated to 40 mbar prior to sealing.

The cathode $Li(Ni_{0.8}Mn_{0.1}Co_{0.1})O_2$ (NMC 811) employed as the active material (97.04 wt%) in this study was double-side coated on 12 µm aluminum current collector to achieve the target mass loading of 38.18 mg cm^{-2}. After calendering, the coating reached a density of 3.27 g cm^{-3}, yielding a reversible capacity of 204 mAh g^{-1} at 25 °C at a C/3 discharge rate, corresponding to an area specific capacity of 3.8 mAh cm^{-2}.

The anode was composed of a graphite–Si/C composite in which nanosilicon was impregnated into the carbon matrix (81.9 wt% graphite, 14.5 wt% Si/C) and coated on 10 µm copper current collector. The double-side mass loading was 21.28 mg cm^{-2}. After calendaring to a density of 1.6 g cm^{-3}, the anode exhibited a reversible capacity of 564 mAh g^{-1} under the same testing conditions, corresponding to an area specific capacity of 4.5 mAh cm^{-2}.

For Type 1 cells, one side of the anodes was removed (also referred to as "decoated") prior to cell assembly. To achieve this, a DSA sheet was taped down onto a flat surface and the top layer was manually decoated with the use of water. During the cell assembly, the anode was deliberately oversized relative to the cathode in terms of the area and area specific capacity, yielding a negative-to-positive capacity ratio (N:P) in the range of 1.13–1.17. All electrode and cell specifications are summarized in Table 1.

2.2. Measurement setups

2.2.1. Pneumatic presses

Actively controlled in-house developed pneumatic presses (denoted as "cell presses") were used for constant-force swelling measurements. The press design, including its control architecture and calibration methodology, has been described in detail in previous publications by Deich and von Kessel [8,12], and is illustrated in Fig. 1 **(b)**. It supports

Table 1
Specification of Type 1 (~180 mAh, sandwich-type) and Type 2 (~3.2 Ah, multilayer) pouch cells.

	Units	Type 1	Type 2
Nominal capacity	Ah	0.18	3.2
Number of cathode/anode layers		1 DSA / 2 SSA	5 DSC / 6 DSA
Cell thickness (dry components)	mm	0.589	1.968
Cell thickness (filled and compressed)	mm	0.591	1.982
Cathode dimensions	cm	4.8 × 4.8	8.2 × 10.55
Anode dimensions	cm	5 × 5	8.6 × 10.9

	Units	Cathode	Anode
Active material		NCM811	Si/C, C
Active material content	%	97.04	14.5, 81.9
Specific capacity	mAh g^{-1}	204	564
Coating loading	mg cm^{-2}	19.1	8.1
Areal capacity	mAh cm^{-2}	3.8	4.44
Density after calendaring	g cm^{-3}	3.28	1.6
Thickness of current collector	µm	12 (Al)	10 (Cu)
Thickness of the coating	µm	58.5 (SSC)	50.5 (SSA)

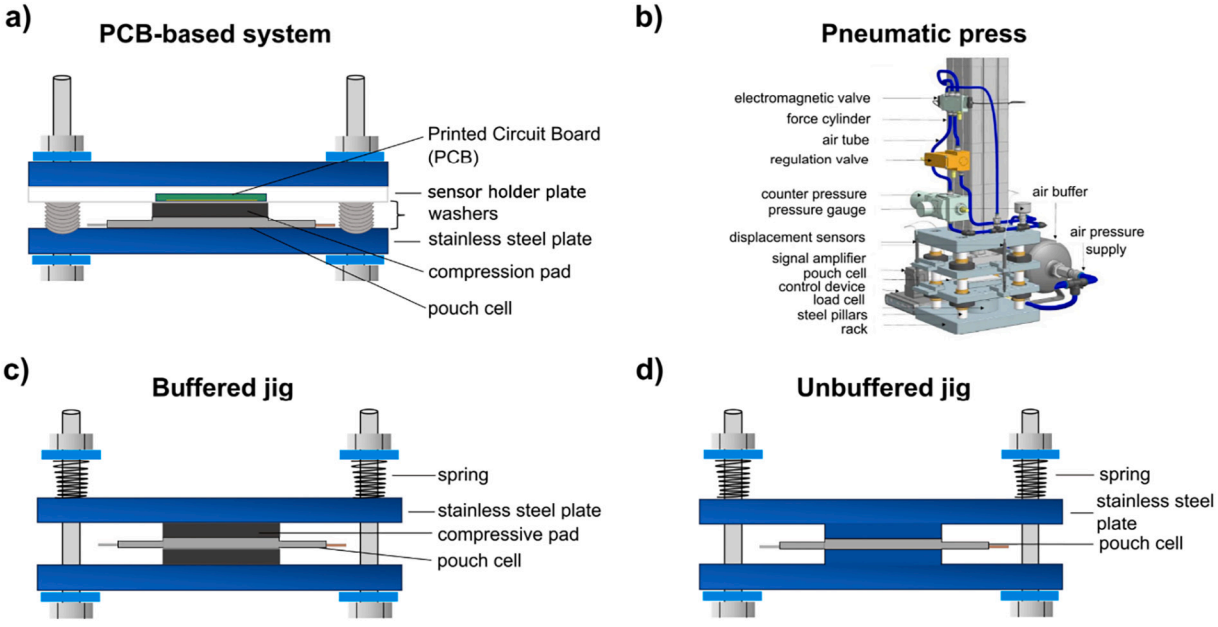

Fig. 1. Measurement setups overview: a) PCB with eddy-current sensors, b) pneumatic press, c) jig with the compression pads (buffered) and springs, d) jig with hard plates (unbuffered) and springs.

operation under constant or variable force with a force accuracy of <1% or in in stiffness control mode enabling the simulation of constant or variable stiffnesses, including constant-gap mode. The system can apply forces from around 100 N up to 16 kN, making it suitable for characterizing mechanical boundary conditions in battery cells. The press consists of four vertically aligned metallic plates (200 mm × 250 mm). The cell press was initially designed for the large-format cells (Type 2), however over time the system was adapted to accommodate the smaller Type 1 cells. Two custom-made spacer plates (60 mm × 55 mm) and corresponding POM-C fixtures were fabricated and positioned on the main plates. These fixtures ensured repeatable placement of the small-format cells in the center of the press while preventing unwanted cell movement when closing the cell presses.

Prior to the start of the experiments, all cell presses were calibrated through repeated stiffness tests. Three measurements were conducted across a force range of 100 N to 3 kN (for the small press setup) and up to 16 kN (for the standard configuration). The calibration curve was implemented in the control software to correct for the intrinsic deformation of the pressing plates during measurements. Before each test, the displacement and force sensors were zeroed. Cells were mounted centrally on the lower press plate, and an initial preload of 100 N was applied. Following, the target force was applied, and a 12-h rest period was initiated – aligned with the initial resting phase of the formation procedure. All measurements were conducted in a climate chamber (Memmert IPP 750) maintained at a constant temperature of 25 °C.

In Type 2 cells, four tapes (two on the top and two on the bottom, on both sides) were applied around the stack to prevent shifting. To avoid exerting pressure on the thickest areas of the cells, a cut-out aluminum foil template was prepared. A pressure sensitive foil was then applied to confirm a uniform pressure distribution across the stack area. In Type 1 cells, the tape was applied on the oversized separator outside the stack area.

2.2.2. PCB-based eddy-current sensor setups

PCB-based eddy-current displacement sensor setups were employed for quasi-constant force swelling measurements. A detailed sensor design and functionality were previously introduced by Brauchle et al. [32,33]. The system features a copper coil and a concentric capacitor forming a resonant LC circuit. The coil generates an alternating magnetic field that induces eddy currents in nearby conductive materials, such as the aluminum pouch cell housing. The resulting opposing magnetic field modulates the circuit's inductance, leading to measurable frequency shifts that correlate with thickness changes of the medium (compression pad) between two conducting surfaces. The compression of the foam, and thus the pressure on the cell, is defined by fixing the distance between the top and bottom plates using precision-manufactured washers of different thicknesses (0.1, 0.3, 0.5, and 1 mm). This distance is chosen to account for both the thickness of the cell and of the compressed foam. The top plate is then lowered using a screwdriver until it meets the resistance provided by the washers, and the resulting compressed foam applied a quasi-constant force to the cell. The foam compressibility and their force response are described in section 2.3 and a schematic of the PCB setup is shown in Fig. 1 **(a)**.

2.2.3. Reference jig fixtures

Two additional fixture setups or jigs were implemented to serve purely as cycling reference cases, however neither of them was designed for the in-operando thickness measurements. Each consisted of two vertically aligned metal plates, movable in the z-direction and held under quasi-constant force load using compression springs (Fibro, DIN ISO 10243). In one configuration, compression pads were attached to the center of both plates, facing the cell surface (buffered). In the other configuration, the plates made direct contact with the cell active area (unbuffered). The spring dimensions and stiffness were chosen to achieve target pressure levels, which were estimated based on the distance the spring was compressed or extended from its original and spring constant. These setups were not equipped with thickness sensors, but instead, they were used to assess the influence of bracing conditions, specifically the presence or absence of buffering elements, on overall electrochemical performance during cycling. Both schematics with and without the foam are depicted in Fig. 1 **(c)** and Fig. 1 **(d)**, respectively.

2.3. Compression pad characteristics

In the PCB-based setup, the distance between the sensor and the pouch cell surface is maintained using an open-cell polyurethane (PU) compression battery pad (PORON EVExtend, Rogers Corporation). As reported by Brauchle et al. [32], optimal sensor resolution (below 4 nm) is achieved when the distance between two conducting surfaces lies in the range of 2–3 mm. Therefore, the foam must maintain thickness within this target range under compression. Additionally, keeping the foam within its compressibility window is essential to ensure a quasi-constant pressure regime [27,34]. Beyond this threshold, the foam exhibits increased stiffness and permanent deformation, which deteriorates pressure reproducibility and sensor accuracy. To ensure compliance with both criteria, three foam materials with initial (uncompressed) thicknesses of approximately 3 mm were selected for evaluation. Other material properties such as mass and thickness were summarized in **Fig. S1 (a) – (b)**. The densities and mechanical behavior of each foam were presented in Fig. 2 **(a) – (b)**. Foam Type 1 and 3 had the same chemical formulation but a different density: 500 kg/m^3 and 380 kg/m^3, while Type 2 had a different chemical formulation with a density of 400 kg/m^3. The mechanical behavior was characterized by using CFD (Compression Force Deflection) and applying a displacement-controlled compression and decompression cycle at a fixed rate of 0.1 mm/min in 3–1.6 mm range in the pneumatic press. Each cycle was repeated twice on the same foam sample to assess reproducibility and hysteresis. CFD is a typically performed test for elastomeric materials, which indicates its capability to withstand compression. The foam that presented the most favorable results in terms of stability over the wide range of pressures (~170–500 kPa) and the highest density was Foam Type 1, and therefore it was selected for further characterization.

2.3.1. Calibration curves

Three distinct calibration protocols were implemented to characterize the behavior under compression of Foam Type 1, which results are depicted in Fig. 2 **(b)**:

- Compression Force-Displacement (CFD) curve – the method was described in the previous section.
- Stepwise compression with rest periods (one foam sample for all steps) – A single foam sample was compressed in 0.1 mm steps starting from 2.9 mm down to 1.7 mm, following progressive compression. Each compression step was held constant for 12 h, simulating the cell resting time prior to the cell formation. Force data was continuously recorded, and only the final value at the end of each 12-h interval was used to construct the calibration curve.
- Stepwise compression with rest periods (a new foam sample for every step) – The same compression protocol and gap range as in method 2 were applied, but each compression step used a new, uncompressed foam sample. This method captures the initial dynamic compression response of the foam under an immediate load and best replicates the real conditions in the PCB setup, where the foam is compressed instantaneously.

Fig. S2 (a) – (b) presents exemplary calibration curves showing the raw force data before conversion to the pressure–foam thickness relationship.

2.3.2. Foam relaxation behavior

Foam relaxation under static compression is a critical factor influencing long-term accuracy to correctly characterize cell swelling

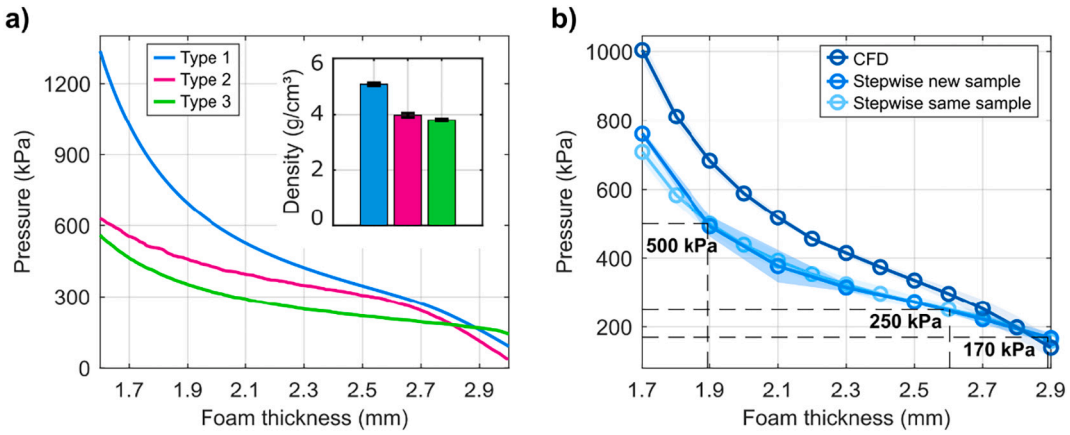

Fig. 2. Compression pads mechanical characterization including: a) Compression Force Deflection (CFD) of all three foam types, b) three methods of establishing the calibration curve for the selected Type 1 foam.

behavior. Immediately after compression, the foam exhibits a very pronounced stress relaxation due to the initial dynamic decompression response, followed by slower decay over an extended period. To quantify this behavior, a series of blank tests were conducted in the PCB setup, where no current was applied, and the results are presented in Fig. 3**.** The pouch cells, identical to those used in swelling tests, were compressed together with foam to three different thicknesses that corresponded to three different pressures – 170, 250 and 500 kPa. These pressures were selected based on the best practices for Si/C-containing anodes according to the literature [4,18,35].

The resulting data reflect only the time-dependent relaxation of the foam, with no cell expansion contributions. Based on these results, the timeline was segmented into three distinct phases:

1. 0–12 h: Initial cell relaxation phase prior to formation
2. 12–155 h: Cell formation, mid-term relaxation
3. 155–1300 h: Long-term cycling, long-term relaxation

Data in each timestamp were normalized to their respective initial time point (0, 12 and 155 h) to isolate the relative relaxation behavior, which was later used for the estimation of the fitting function and data correction in section 3.1.2. This study serves as a guideline for establishing a data analysis procedure using PCB-based setups to measure relative thickness changes. A representative pressure of 250 kPa was selected after extending the experiments to include swelling and electrochemical testing at 170, 250, and 500 kPa over 400 cycles. While the capacity retention was nearly identical across all three pressure levels, a pronounced reduction in the breathing amplitude was observed at 500 kPa (see Fig. 3 **(b)**). This suppression of reversible thickness changes at higher pressure motivated the selection of 250 kPa as a representative condition for our methodology. A direct comparison between relaxation characteristics and in-operando swelling response during cycling at three pressures can be found in section 3.1.1 together with a more detailed pressure selection explanation.

Mid-term foam relaxation behavior (0–155 h, equivalent to cell relaxation and formation time) was also validated at the representative pressure of 250 kPa: in the pneumatic press (Fig. 4), and in the PCB setup using the TekScan Pressure Mapping Sensor 5040 (Fig. 3S **(a)-(b)**). The pressure sensitive sensor foil was previously calibrated to 250 kPa in the cell press. In the first case, the demonstration was performed in the constant-gap mode in the cell press at 2.6 mm compression, which according to the calibration curve corresponds to 250 kPa. The constant-gap mode was applied to the foam sample and was kept for 155 h. The final force was utilized to calculate the force retention compared to 12-h time (reference to the beginning of the formation). In the second experiment, the cell with mapping sensor and the foam were placed in the PCB setup accounting for the thickness of all components. Firstly, a blank test was performed, where no current was applied to the cell, and foam relaxation together with the sensor drift was captured. Finally, the cell formation was conducted and the resulting force on the pressure foil sensor was recorded.

2.3.3. *Data analysis procedure*

To decouple true cell dilation from foam relaxation, a structured

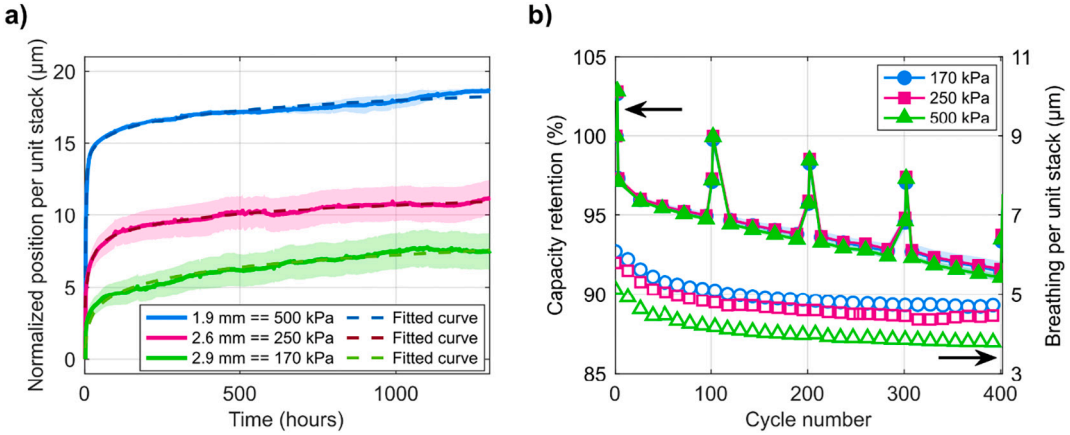

Fig. 3. Mechanical and electrochemical performance comparison utilizing Type 1 foams at three different pressures (170, 250 and 500 kPa) in the PCB setups: a) long-term relaxation, b) capacity retention (filled markers) and breathing (unfilled markers) during cycling.

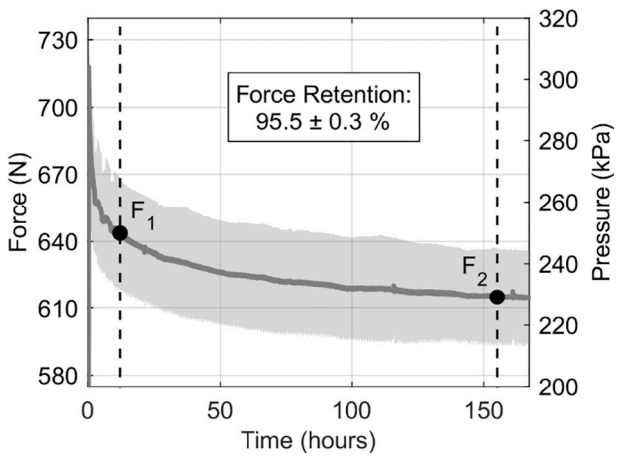

Fig. 4. Pressure validation and force retention in the constant-gap mode in the pneumatic press recorded at 250 kPa.

four-step data analysis procedure was developed and applied to a representative test cell. The results of the formation are presented in Fig. 5 **(a)** and for combined formation and cyclic aging in Fig. 5 **(b)**:

1. Raw Data Extraction

Sensor output data was extracted from four individual eddy-current sensors and matched with the timestamps from the corresponding electrochemical data.

2. Normalization

Each sensor signal was normalized to its initial value to track relative thickness changes while converting raw values with offset to a relative scale starting from 0.

3. Averaging and Initial Fit

The normalized data from all four sensors were averaged. During the first 12 h (cell preconditioning), any thickness change is attributed to foam relaxation. A suitable fitting function was applied to this region to model the long-term relaxation curve.

4. Data Correction

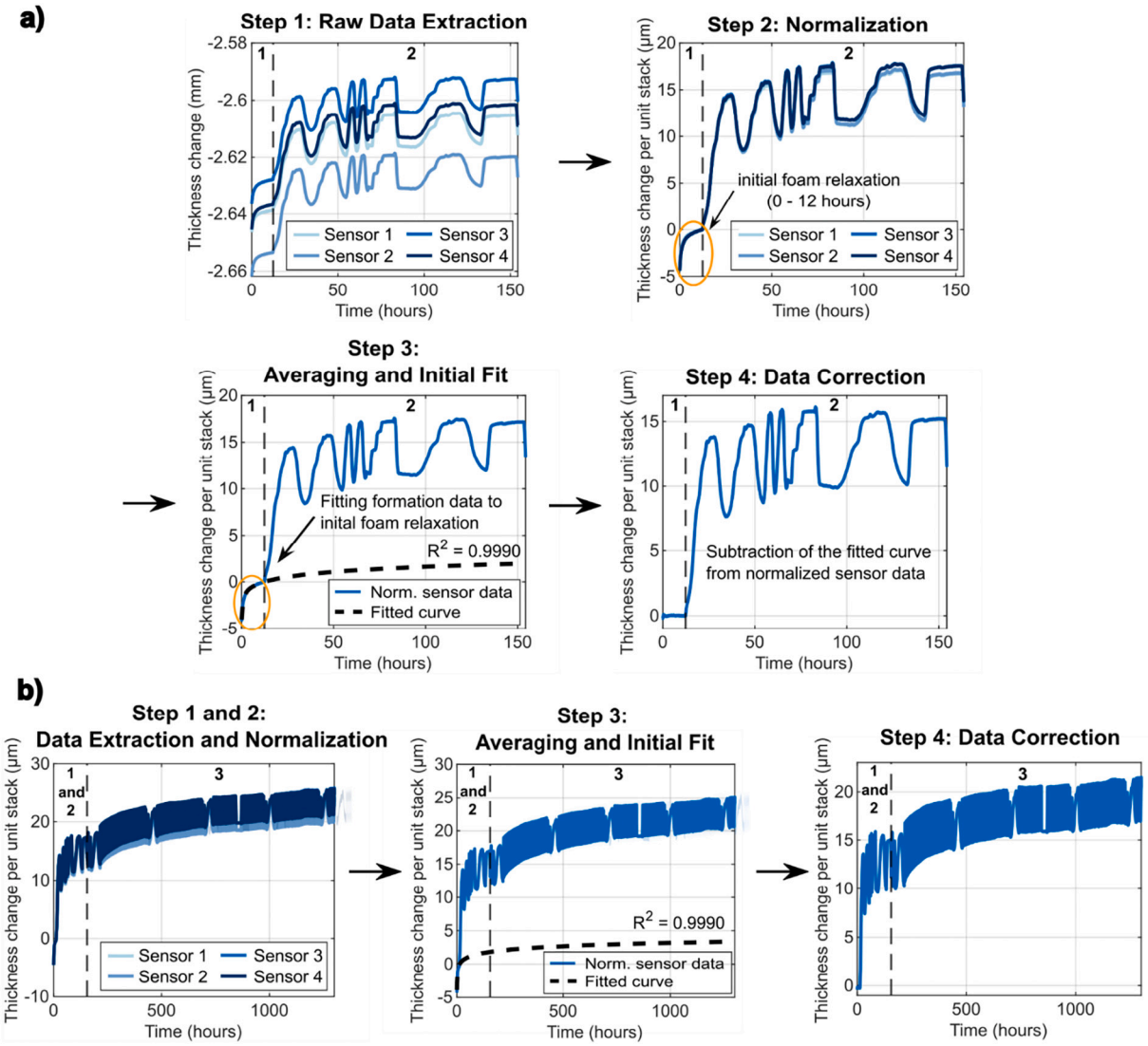

Fig. 5. Detailed steps with data analysis workflow for: a) formation results, b) combined formation and cycling results, including raw data extraction, normalization, averaging and initial fit, data correction steps. The figures were split into 3 phases: phase 1 – cell wetting and relaxation, 2 – cell formation, 3 – cell cycling.

The fitted relaxation curve was subtracted from the entire dataset to isolate the foam contribution from cell expansion.

2.3.4. Foam behavior under different mechanical boundaries

In the last step of the analysis of the compression pads, three curves from different measurements performed at around 250 kPa, were brought together and their shapes were compared in Fig. 6. An overlay of three independent curves was plotted – 1) foam relaxation in the PCB setup from **Figs. 3**, 2) foam relaxation in the pneumatic press from Fig. 4 **(a)** and 3) the fitted curve during cell formation in the PCB setup from Fig. 5 **(a)**. For PCB-based tests, the monitored metric was the thickness change in mm, whereas in the cell press it was the force change in N. Since these variables cannot be directly compared and there was a downward trend observed in the cell press results, the data was inverted and scaled to align numerically with the range of the thickness tests for direct comparison.

2.4. Testing procedure

All electrochemical tests were performed using a battery cycler (CTS, BaSyTec, Germany) inside a temperature-controlled chamber (Memmert IPP 750) maintained at 25 °C. The test protocol included an initial cell preconditioning, followed by formation and cyclic aging procedures. The exact phases and parameters including the C-rates and voltage cutoffs are provided in Table 2.

2.4.1. Formation

The formation consisted of 6 cycles and lasted approximately 155 h. It began with a 12-h relaxation and wetting phase at 1.5 V. This was followed by two C/10 and one C/3 cycles. Next, the RPT was performed (see section 2.4.3) and finally, the cell was charged up to SoC 75% and left at rest for 18 h to determine the self-discharge rate (SDR). During this period voltage decay was monitored, where a high rate of voltage drop can indicate potential parasitic effects such as separator defects, or high internal self-discharge currents. After the SDR test, the cell was discharged to SoC 30% at C/3 rate to prepare for the cyclic aging phase.

2.4.2. Cyclic aging

The cyclic aging was divided into two phases: a reference performance test (RPT) every 100 cycles and a continuous cycling phase. The procedure commenced with an initial RPT to establish the begin-of-life (BOL) reference. Following this, the cell underwent 98 continuous charge-discharge cycles following a cycling protocol shown in Table 2.

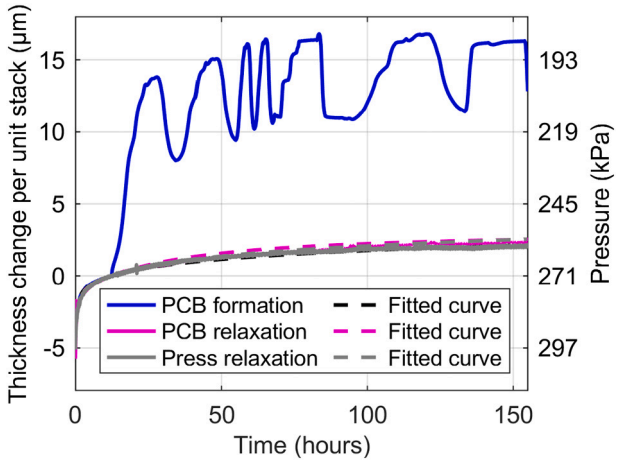

Fig. 6. Fitting of experimental data to the empirical fit for: uncorrected formation PCB data, PCB relaxation curve, force relaxation in the pneumatic press. The measurements were performed at the constant gap of 2.6 mm (250 kPa) in both pneumatic press and PCB systems.

Table 2
Test procedure including formation and cycling.

Phase	Charge		Discharge	
	C-Rate	Voltage/SoC	C-Rate	Voltage
Formation				
Rest	C/20 CC	1.5		
1st step	C/10 CCCV	4.25	C/10 CC	2.5
2nd step	C/3 CCCV	4.25	C/3 CC	2.5
DCIR test	1 CC	25%, 50%, 75%	C/3 CC	2.5
3rd step	C/20 CCCV	4.25	C/20 CC	2.5
SDR test	C/3 CCCV	75%	C/3 CC	3.5
Cycling				
1st step	C/3 CCCV	4.25	C/3 CC	2.5
DCIR test	1 CC	25%, 50%, 75%	C/3 CC	2.5
2nd step	C/20 CCCV	4.25	C/20 CC	2.5
3rd step	1 CCCV	4.25	1 CC	2.5

After every 100 cycles, an RPT was performed to track capacity retention, resistance development, and overall performance degradation over time. This sequence was repeated until the targeted 408 cycles count was reached or until predefined end-of-life (EOL) criteria were met (i.e. 80% SoH).

2.4.3. Reference performance test

Each RPT consisted of a C/3 charge and discharge cycles, a direct current internal resistance (DCIR) test and a C/20 charge and discharge cycles. The DCIR test was conducted with a 1C charge and 1C discharge pulse lasting 30s at 3 different SoCs (25%, 50% and 75%). The SoC levels were determined based on the actual C/3 discharge capacity in each RPT and set using a charge current at C/3. After the final pulse, the cell was charged to 100% SoC using a C/3 rate, followed by a 6-h rest period.

2.5. Evaluation methodology

2.5.1. In-operando swelling

For in-operando swelling measurements, the thickness change data was compared for all three setups over the 408-cycle range and the results are demonstrated in Fig. 7 **(a)-(d)**. Both irreversible and reversible thickness changes were analyzed. The irreversible change corresponds to the minimum dilation reached during each discharge cycle, which contributes to the irreversible thickness growth. The reversible change represents the difference between the maximum and minimum dilation within a single discharge cycle, capturing the so-called "cell breathing" – the periodic expansion and contraction of the cell during lithiation and delithiation according to the equation:

$$d\_breathing_i = d\_max_i - d\_min_i \quad (1)$$

where d is dilation, and i is the selected cycle.

For specific RPT cycles, the dilation peaks were analyzed with a primary focus on their key features such as cell breathing and the characteristic dilation shapes. In the PCB-based swelling measurements, the foam relaxation correction procedure was executed prior to obtaining cell swelling results. Furthermore, the study systematically compares the influence of mechanical constraints, including compression pads and rigid plates, on both electrochemical performance and mechanical (swelling) responses throughout formation and long-term cycling.

2.5.2. Electrochemical performance

In this study, the impact of the test bench on electrochemical degradation was assessed by comparing capacity retention and DCIR evolution across different cell configurations. Capacity retention, defined as the ratio of remaining capacity to the first cycle capacity at 1C charge and 1C discharge rates, served as a primary indicator of cell aging. It reflects the state of health (SoH), which was calculated using

the relation:

$$SoH_i = \frac{Q_i}{Q_0} \cdot 100\% \quad (2)$$

where Q_0 is the initial capacity, and Q_i is the capacity in cycle i.

In addition to capacity fading, DCIR was also monitored as another degradation metric, measured during regular RPT check-ups (test specification was provided in section 2.4.1). It is calculated as the voltage response from the cell at a defined current pulse and divided by the applied current. Precisely, it is determined by measuring the voltage drop at the beginning of the discharge pulse and the voltage after 10s, then dividing this voltage difference by the applied current. In this study, the selected discharge pulse at 50% SoC was evaluated after 10s as shown here:

$$DCIR_{t=10s} = \frac{U_{t=0s} - U_{t=10s}}{I} \quad (3)$$

where $U_{t=0s}$ is the last voltage value before pulse, $U_{t=10s}$ is the voltage value at 10 s of pulse, and I is the current pulse.

3. Results and discussion

3.1. Compression pads

Viscoelastic materials such as the compression pads used in this study can exhibit significant microstructural variability, even when bulk properties like mass loading or density remain consistent. These internal differences can influence mechanical behavior such as compression response, relaxation dynamics, and long-term stability [22,27]. Therefore, to ensure statistical reliability and account for this inherent variability, repeated measurements and reporting of standard deviations are essential.

3.1.1. Calibration curves and relaxation

Among the three calibration protocols shown in Fig. 2 **(b),** the "stepwise compression new sample" method was selected primarily because it most closely mimics the actual PCB measurement procedure: the compression distance is preselected, the plates are immediately set to this distance, and after each measurement the foam is replaced with a new sample. Quantitative comparison with the "stepwise compression using the same sample" method shows only minor differences in force (e.g. <3% at 2.6 mm foam thickness), indicating that both protocols produce similar mechanical responses. It is suggested that the compression pads retain their ability to apply consistent pressure without significant material degradation, even under increasing compression and over extended time. However, from an experimental point of view, using a new sample for each step is more appropriate, as it avoids potential memory effects and better reproduces the PCB measurement conditions. While CFD is a standard characterization metric for elastomeric materials, it offers limited applicability here due to the rapid increase in applied force, which masks gradual relaxation behavior.

Based on stepwise compression with rest periods (a new foam sample for every step) calibration curve, three target pressures were selected for understanding the relaxation behavior: 170, 250, and 500 kPa, corresponding to foam thicknesses of 2.9, 2.6, and 1.9 mm, respectively. Firstly, a series of blank tests were conducted to examine the long-term foam relaxation with regard to four previously described time windows: 0–12, 12–155, 12–1300, 0–1300 h. Prior to each new PCB-based test, a fresh foam sample was characterized in terms of mass and thickness to ensure consistency within predefined ranges. For each pressure condition, at least three individual measurements were conducted and averaged with standard deviations, which are shown in Fig. 3 **(a)**. The recorded thickness data occasionally exhibits characteristic irregularities at specific time points, which may be influenced by external disturbances, such as door openings. Additionally, the temperature sensitivity of the eddy current sensors and its effect over time was evaluated for one of the relaxation tests measured at 250 kPa and is presented in **Fig. S4 (a)-(b)**.

As shown in **Fig. S4 (a)**, the thickness follows the expected relaxation behavior, characterized by a gradual increase over time. The temperature fluctuations recorded by the sensor (purple curve, right axis) show only minor deviations with an amplitude below 1 °C, representing a small overlay on top of the general relaxation trend. A temporary temperature drop observed at around 600 h does not have a lasting influence on the thickness evolution, as the relaxation continues to follow the same increasing trend. The effect of these short-term temperature variations is illustrated in the magnified view of the highlighted region between 250 h and 350 h in **Fig. S4 (b)**. The correlation analysis indicates that these temperature-induced signal perturbations are small and transient, with no significant effect on the overall relaxation trend of the stack thickness. Within the 250–350 h window, the cross-correlation between temperature and thickness change reached $r = 0.97$, confirming a strong linear dependency. A linear fit yielded a thermal expansion coefficient of approximately 0.156 μm/°C, indicating that temperature fluctuations have a negligible effect on thickness changes. Therefore, no additional temperature compensation was applied.

The results in Fig. 3 **(a)** reveal a pronounced foam relaxation during the first 12 and 155 h due to the rapid decompression and a progressing creep, which stabilizes significantly beyond that point toward the end of the test. Each of the mean experimental plots were fitted with the same 5-parameter empirical fit for the whole data range, which is described in section 3.1.2 and the results can be found in **Table S1**. The mean values and standard deviations of the relaxation curves were summarized in Table 3. All data are normalized per unit stack to allow comparison across cells with varying numbers of stacks (i.e. Type 1 and 2). Relaxation during the initial 0–12 h was greatest at highest compression (1.9 mm) and the lowest at 2.9 mm. In other words, the absolute recovery right after decompression is larger for higher compressions, which is an expected phenomenon for viscoelastic materials. Both 1.9 mm and 2.6 mm compressions presented similar relaxation behavior in 12–155-h time window. During the extended testing phase (equivalent to formation and cycling time), the relative thickness change is very similar across different compressions.

Following the detailed evaluation of foam relaxation behavior in Fig. 3 **(a)**, the same pressure conditions were applied in long-term cycling tests to assess their influence on electrochemical performance and breathing behavior, as shown in Fig. 3 **(b)**. The cycling protocols, cell compositions, and experimental conditions were identical to those described in Sections 2.1 and 2.4, ensuring that any observed differences arise solely from the applied mechanical boundary conditions. With increasing applied pressure, the breathing magnitude is progressively suppressed, indicating that higher compression constrains the reversible expansion and contraction of the cell during cycling. At 500 kPa, the cells exhibit a reduced breathing amplitude accompanied by a slightly lower capacity retention compared to lower pressure conditions. While the differences in electrochemical performance between 170, 250, and 500 kPa are relatively small and within experimental scatter, the data indicates a modest trend toward increased capacity fade at higher pressure. Overall, these results suggest that moderate pressure does not significantly compromise electrochemical stability while effectively limiting mechanical expansion. In addition, as shown in the pressure – foam thickness calibration curve (Fig. 2(b)), 250 kPa lies closer to the plateau region, where variations in foam thickness result in more constant applied pressure. This suggests that, compared to 170 kPa, a pressure of 250 kPa may offer improved long-term pressure stability. For this reason, 250 kPa was selected as the primary testing pressure for the comparison of the two independent measurement methods for in-operando swelling analysis in this study. Nevertheless, all three pressure levels provide comparable electrochemical behavior while successfully limiting electrode breathing.

Fig. 4 presents the mean data and its standard deviation from three

Table 3
Long-term foam relaxation results applied per unit stack and normalized in four time windows: 0 to 12, 12 to 155, 12 to 1300 and 0 to 1300 h.

Foam compression	0–12 h			12–155 h			12–1300 h			0–1300 h		
	mean (μm)	SD (μm)	SD (%)	mean (μm)	SD (μm)	SD (%)	mean (μm)	SD (μm)	SD (%)	mean (μm)	SD (μm)	SD (%)
1.9	13.6	0.6	4.1	2.6	0.3	9.5	5.0	0.2	4.0	18.6	0.2	1.1
2.6	6.2	0.7	10.6	2.9	1.0	34.2	5.1	1.3	25.0	11.2	1.3	11.3
2.9	3.0	0.6	18.7	1.9	0.9	47.8	4.5	1.3	27.7	7.5	1.3	16.7

independent measurements with the compression pads held at a 2.6 mm constant gap (corresponding to 250 kPa) in the cell press while recording the force change over time. Two force values – F_1 (at 12 h) and F_2 (at 155 h) – represent the start and end of formation, respectively. The initial force reflects the foam's elastic decompression, and as the material undergoes viscoelastic relaxation, the force gradually decays, even though the gap remains fixed. The force retention at F_2 was equal to 95.5% ± 0.3%, indicating that the observed force decay over 155 h has a minimal effect on the foam's force retention capabilities. In this setup, decreasing force over time reflects internal stress relaxation of the foam, not a change in thickness. Since the most significant relaxation occurs early and gradually diminishes over time, the foam can be considered a resilient material. It maintains a quasi-constant force under compression, while the gradually decreasing slope indicates continuous viscoelastic creep over the observed period.

Furthermore, relative pressure changes during formation and cycling in the PCB setup were captured using pressure mapping sensors, as shown in **Fig. S3 (a)-(b)**. The results show that the total pressure increase after formation equals to approximately 10 kPa, reflecting the significant irreversible cell growth occurring during this initial phase. This aligns with expectations, as formation induces substantial electrochemical and mechanical changes, such as SEI formation and gas evolution, which contribute to internal pressure build-up. On the other hand, the average pressure variation during cycling was equal to around 3 kPa. These periodic fluctuations represent the reversible breathing behavior of the cell, primarily driven by lithiation and delithiation processes. Notably, the amplitude and shape of the pressure cycles remain highly stable, indicating that no significant additional pressure build-up occurs at the beginning of cycling.

3.1.2. Data analysis

After detailed calibration and foam characterization, the formation and cycling experiments were carried out using both the cell press and PCB-based setups. For the PCB measurements, data analysis followed the workflow with four key steps, illustrated in Fig. 5 **(a)-(b)**. In Step 3, an empirical five-parameter composite fitting function was applied:

$$y = A \bullet \left(1 - exp^{(-b \bullet t)}\right) + C^{*}log\left(1 + t^{d}\right) + E \quad (4)$$

where t is time and A, b, C, d and E are the fitting coefficients.

The five-parameter model (**Eq. 4**) was selected because the foam relaxation curves exhibit two distinct time regimes: (i) a rapid initial decay and (ii) a slow, quasi-logarithmic long-term relaxation. Classical linear viscoelastic models (e.g., single or double Maxwell/Voigt elements) could not simultaneously capture both regimes in a single analytical form. The adopted function therefore combines:

(a) an exponential term representing short-time viscoelastic relaxation, analogous to discrete relaxation modes in Maxwell-type elements; and.
(b) a logarithmic term representing slow creep, commonly associated with broad relaxation spectra and aging phenomena in polymeric materials.

This composite approach aligns with established viscoelastic modeling strategies, where exponential terms describe reversible relaxation and logarithmic or power-law terms capture long-term, diffusion-limited, or structural evolution processes [36,37]. Similar formulations have been applied to polyurethane foams under cyclic loading and to battery compression pads experiencing irreversible swelling [38,39].

Physical interpretation of the parameters:

A: Maximum reversible deformation (foam compliance under initial stress).

b: Relaxation rate constant, related to the viscoelastic time constant.

C: Magnitude of irreversible growth, linked to swelling and creep.

d: Controls curvature of the logarithmic term, analogous to a creep exponent.

E: Initial offset, representing pre-compression or assembly preload.

To verify applicability for long-term cycling, the fitted parameters were extrapolated to extended time periods ($\leq$ 1300 h) and compared to independent relaxation tests. The model maintained $<$ 2% deviation for the relaxation curve at 250 kPa (Fig. 6), demonstrating robustness in capturing both short- and long-term mechanical behavior. These results indicate that the combined exponential-logarithmic form effectively represents the dual nature of foam deformation under battery-induced stresses.

Fitting was restricted to the first 12 h of each test to isolate the mechanical relaxation behavior of the foam from the electrochemical effects. While the relative thickness changes during the initial decompression phase ($0-12h$) are not the primary focus for curve validation, the overall shape of the fitted function and how it progresses over time is critical. Sensor delays and sample-to-sample variability can influence the decompression rate during the early relaxation phase, potentially leading to variations in the fitted results. To improve consistency across multiple tests, the first hour of data is usually excluded from the fitting process.

While Steps 1 and 2 of the data analysis procedure are relatively robust, Steps 3 and 4 require more careful attention. The selection of the fitting range for the initial relaxation phase is particularly important, as it directly affects the long-term results. In the final step, it is essential to assess whether the fitted curve is physically meaningful. This is where the relaxation results presented in Table 3 become useful. The results are split into four time intervals, however the data from the 12–155 h (formation) and 12–1300 h (cycling) ranges should be compared with the fitted experimental results. Although exact matches are not expected, significant deviations should be avoided. Given the relatively high standard deviations observed in the relaxation data, this variability must be considered when characterizing the mechanical behavior of the polyurethane foams.

To enable direct comparison, three representative curves were plotted over a 155-h window: (1) foam relaxation in PCB, (2) foam relaxation in press, and (3) formation swelling in PCB, as shown in Fig. 6. The composite exponential–logarithmic function was applied to the 0–12 h range in all cases, with independently optimized coefficients (**Table S2**). The fitted parameters were highly consistent, confirming strong similarity between the datasets. Initially, the press and PCB measurements exhibited comparable trends, but deviations appeared at

later times, where the experimental data did not fully overlap with the fitted PCB relaxation data. Meanwhile, the press experimental data remained well aligned with the fitted curve from PCB formation swelling. Furthermore, the PCB formation swelling closely matched the 0–12 h regime, demonstrating that the exponential term accurately captures the rapid initial relaxation.

In the PCB setup, foam relaxation remains largely unaffected by cell expansion during the early phase. At longer times (>12 h), however, swelling gradually constrains the foam's ability to decompress, leading to a mild suppression of relaxation. The deviation between fitted formation and experimental relaxation data is negligible (≈ 0.15 μm at 155 h), especially relative to the foam thickness (2.6 mm).

In conclusion, the three tests addressed complementary aspects of the system: foam relaxation (via thickness and force) and electrochemical swelling. Despite measuring different physical quantities and, in some cases, distinct physical phenomena, they consistently reveal the same underlying phenomenon of the viscoelastic relaxation of the foam under constant compression.

3.2. Cell swelling

The main objective of this study was to compare swelling behavior at the same pressure of 250 kPa across two independent measurement setups: the PCB-based and press-based systems (Fig. 1 **(a)** and **1 (b)**, respectively) and between two different cell formats: Type 1 and 2. Herein, key parameters such as breathing, irreversible thickness changes, and dilation hysteresis shapes were evaluated over cycle life including repeated 1C and C/20 charge–discharge cycles. Additionally, the influence of mechanical boundary conditions was investigated by comparing electrochemical performance between configurations using compression pads and rigid plates (section 3.3). This comparison was conducted using additional reference measurement setups in fixture jigs, one with a compression pad and one without (Fig. 1 **(c)** and **1 (d)**, respectively).

Long-term swelling results per unit stack at 250 kPa for both cell types and setups are presented in Fig. 7 **(a)** showing the minimum and maximum thickness values of the dilation cycles at 1C rate (left y-axis) coupled with breathing results (right y-axis). A zoomed-in view of the formation swelling data (with marked four formation phases described in Table 2) shows a great correlation in values and shapes of the dilation swelling behavior. Over the cycle life all tests follow the same continuously increasing trend with shapes and values closely related to each other validating that both formation and cyclic swelling can be well characterized independent of the measurement device. The data from both setups show good agreement, with only minor deviations observed falling within the standard deviations.

In the first 100 cycles for larger format cells (Type 2) the absolute thickness change per unit stack was slightly higher than for sandwich-type cells (Type 1). We correlate that the difference in the initial cycles is predominantly due to particle rearrangement and binder relaxation [4,40,41]. Additionally, the observed difference in swelling during formation between Type 2 and Type 1 cells can be attributed to cell balancing as Type 2 cells had a slightly lower N/P ratio compared to Type 1 cells (1.15 vs. 1.18). Lower N/P increases the relative utilization

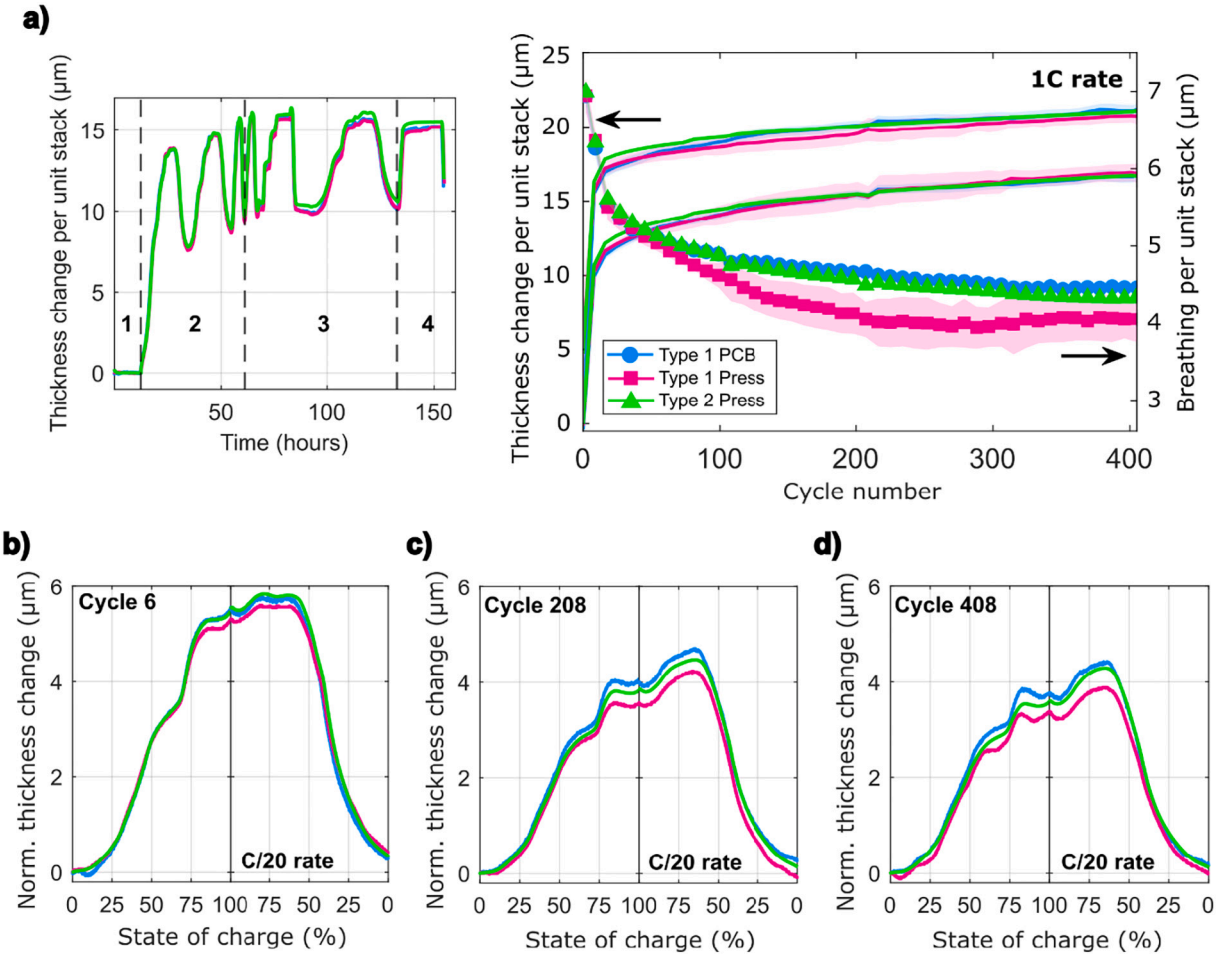

Fig. 7. Swelling analysis of Type 1 and 2 cells in the PCB and cell press setups: a) minimum and maximum of thickness change per unit stack and breathing over cycle life with a close-up on the formation cycles split into 4 phases. Normalized thickness change per unit stack at RPT cycles for b) cycle 6 (formation), c) cycle 208 (cycling) and d) cycle 408 (cycling). All measurements were performed at 250 kPa.

of the anode during formation, which can enhance both reversible and irreversible thickness changes during early cycles (as shown in Cycle 6th in Table 4) [41]. During the consecutive cycles, the cell balancing seems to stabilize as Type 2 Press shows intermediate values swelling results in the maximum and minimum dilation. Although supporting data is limited, we hypothesize that the observed behavior may also arise from anodes not facing cathodes, allowing continued SEI formation and particle rearrangement. These processes may contribute to additional thickness changes that are not observed in the Type 1 cells, which lack terminal electrodes.

Moreover, the breathing behavior is nearly identical for all cell configurations up to approximately 50 cycles. However, beyond this point, a clear differentiation between the results becomes apparent. The Type 1 Press configuration exhibits a distinctly reduced breathing amplitude, which tends to stabilize after around 200 cycles, whereas the Type 1 PCB and Type 2 cells show largely overlapping results. Additionally, **Fig. S5 (a)** illustrates the irreversible thickness growth after formation for the three cell setups. Initially, all cells exhibit similar irreversible growth trends, however, the differences become evident with continued cycling. After 408 cycles, the Type 1 PCB combined with the Type 2 Press configuration shows a strong correlation between capacity retention (see plot and discussion in Section 3.3) and irreversible thickness growth, while the Type 1 Press configuration displays pronounced irreversible growth that is not accompanied by a proportional decrease in capacity retention. These findings suggest that the swelling behavior in Type 1 Press cells, particularly the reduced breathing and increased irreversible component of the thickness growth, contributes to the decreased electrochemical performance observed.

The PCB cell was disassembled after 408 cycles, and the electrode thicknesses were measured to verify whether the external sensor readings accurately reflect changes in electrode thickness. The electrode thickness was determined using a Mitutoyo High Accuracy Digital Micrometer (0–25 mm, model 293–100-20) with a resolution of 0.1 μm, and the results, including standard deviations, are presented in **Table S3**. The measurements were performed under the standard measuring force of the device (7–9 N), corresponding to an applied pressure of approximately 870–1120 kPa based on a measuring face diameter of 3.2 mm. The measured mean thickness change for the single-side coated anode was 24.4 μm, while the double-side coated cathode exhibited a change of −5.2 μm. This corresponds to a total thickness change of 21.8 μm per unit stack, representing a deviation of only ~2.8% compared to the PCB-based measurements. These results demonstrate a consistent trend between the external swelling data and the mechanically determined electrode thickness changes, confirming that the PCB-based external measurement method reliably captures the internal electrode expansion behavior.

Before- and after-cycling SEM images were acquired on a fully delithiated cell to examine particle morphology, coating uniformity, and surface integrity at the center and edge regions of the anodes (**Fig. S6 (a)–(b)**). Additionally, cathode SEM top view and cross-section images (**Fig. S6 (c)–(d)**) were disclosed and the corresponding initial and post-cycling thickness values are reported. For in-situ thickness determination, the distances between the coating edges and the current collector (for double-sided coatings, between the upper and lower coating boundaries) were manually marked on each cross-sectional image and processed in MATLAB using the pixel size specified in the image metadata. Additionally, the in-situ thickness measurements based on the SEM images are challenging due to the spherical and three-dimensional nature of the particles, which makes it difficult to accurately determine the true coating edge from a two-dimensional image.

Cross-sectional SEM analysis showed that the anode coating increased from approximately 52.66 μm (±0.7 μm) before cycling to 70.78 μm (±0.6 μm) after cycling, corresponding to an expansion of 18.12 μm. The cathode thickness increased from 59.13 μm (±1.01 μm) to 60.66 μm (±0.89 μm), resulting in a total change of ~1.53 μm, or 19.65 μm per unit stack. To validate these results, independent micrometer measurements were performed during cell disassembly prior to SEM sample preparation. These measurements indicated an anode thickness increase of ~15.5 μm (±0.1 μm) and a cathode increase of ~1.6 μm (±0.1 μm), corresponding to a thickness change per unit stack change equal to 17.1 μm. Finally, according to Fig. 7(a), the PCB-derived thickness change per unit stack after 408 cycles in the delithiated state was ~17.5 μm. The differences between SEM-, micrometer-, and PCB-based results (2.3% and 12%) are likely attributable to the absence of external pressure during SEM measurements and the inherent uncertainties associated with interpreting coating boundaries in SEM cross-sections. Moreover, it should be noted that micrometer screw measurements effectively capture the maximum thickness over the entire measurement surface (~8 mm^2), whereas SEM-based thickness estimation reflects local thickness variations and surface inhomogeneities at the sub-micrometer scale.

3.2.1. RPT cycles

A more detailed analysis of the mechanical response and the shape of dilation response was conducted at C/20 rate at selected RPT cycles (cycles 6, 208 and 408) and is shown in Fig. 7 **(b) – (d)**. In each case, the thickness change was normalized to the beginning of the respective cycle to facilitate direct comparison. During the formation cycle (cycle 6), a strong correlation was observed across all configurations, both in the characteristic shape of the dilation curves and in the magnitude of thickness changes.

For cycles 208 and 408, a noticeable difference emerged between the Type 1 Press configuration and both the Type 1 PCB and Type 2 Press setups, where the first presents lower dilation values. This trend aligns well with the 1C cycling data shown in Fig. 7 **(a)**, where a similar pattern of reduced breathing was observed in the Type 1 Press configuration. This phenomenon may be attributed to several factors, one of which could be capacity loss. However, accurately identifying the underlying cause would require further investigation, such as differential voltage (dV/dQ) and capacity (dQ/dV) analyses, which falls outside the scope of this study.

Table 4 summarizes the key metrics, including the minimum and maximum thickness of each dilation peak (**Eq. 2**), breathing, and corresponding standard deviations at selected RPT cycles. The press-based (Type 2) exhibited moderately higher breathing results in the 6th and 208th cycles compared to Type 1. Although, the PCB-based setup

Table 4
Swelling results with maximum and minimum thickness change per unit stack, breathing and corresponding standard deviations for the selected RPT cycles.

Cycle	Type	Method	Max dilation (μm)	SD (%)	Min dilation (μm)	SD (%)	Breathing (μm)	SD (%)
6	Type 1	PCB	15.4	1.7	10.0	3.1	5.4	1.2
		Press	15.5	1.2	10.0	1.0	5.5	2.3
	Type 2	Press	16.1	0.3	10.6	0.1	5.6	0.7
208	Type 1	PCB	20.1	1.4	15.7	1.5	4.4	1.3
		Press	19.5	2.7	15.3	3.9	4.2	3.0
	Type 2	Press	19.8	0.8	15.4	1.0	4.4	0.1
408	Type 1	PCB	21.1	1.9	16.8	1.7	4.4	4.2
		Press	20.7	2.3	16.9	3.4	3.8	4.1
	Type 2	Press	20.9	0.7	16.7	0.7	4.2	0.5

showed slightly higher maximum and minimum dilations in cycles 208 and 408, its breathing behavior was very similar to that of the Type 2 Press. Interestingly, Type 1 press results displayed consistently higher standard deviations across all cycles, while Type 2 showed the lowest variability. These observations suggest that the increased number of unit stacks in Type 2 cells contributes to homogenizing local thickness variations across the stack area. Finally, the PCB setup effectively captured the full swelling range with breathing behavior comparable to press-based methods, validating its use for in-operando measurements.

3.3. Electrochemical performance

The results for capacity retention and DCIR development from all tested cells and setup configurations (with the reference tests in the jigs), are presented in Fig. 8 **(a)-(b)**. All of them reached 408 cycles before EoL criteria were met. However, the difference in capacity retention (determined by **Eq. 2**) between the highest-performing configuration (Type 1 PCB and jig with foam) and the lowest-performing one (Type 1 Press and jig without foam) was approximately 4%. Statistical analysis (one-way ANOVA, $F = 12.34$, $p = 0.0017$; Kruskal-Wallis test, $H = 10.16$, $p = 0.038$) confirms that the observed higher capacity retention in foam-buffered setups compared to rigid-plate setups is statistically significant, supporting the conclusion that the foam buffering improves electrochemical performance compared to rigid-plate setups. Moreover, assuming a progressing capacity decay over cycle life, this would bring a relatively high difference e.g. at 1000 cycles. Both configurations utilizing compression pads (Type 1 PCB and the foam-based reference test) exhibit closely matching and less pronounced cyclic aging compared to those employing rigid plates. Overall, the usage of compression pads results in higher capacity retention during cyclic aging, presumably due to a more homogeneous pressure distribution [6,27,28,42]. Notably, the larger format cells (Type 2) tested in the cell press show intermediate behavior, falling between compression-pad and rigid-plate configurations. As previously mentioned, the higher number of unit stacks promotes a more uniform distribution of local thickness variations.

Besides that, several studies have worked on the cell size effect and its influence on the cell's degradation and the influence of thermal effects on cycling performance [43,44]. Previous work from Lin et al. [45] showed that the thermal conductivity in a pouch cell is around 50× times larger in in-plane direction compared to the through-plane direction. Therefore, the large thermal mass of the metal plates has a significantly higher impact on the temperature of the outer electrodes in the cell, which might be less prominent in the setups comprising foams. Thus, in the larger format the inner electrode layers have a more homogeneous temperature distribution compared to thin sandwich-type of cells.

Moreover, the DCIR measurements obtained during the discharge pulse at 50% SoC (according to **Eq. 3**) for all cells were evaluated after 10 s and plotted as an absolute resistance change due to differences in absolute values (Fig. 8(b)). All cells experienced a notable drop in absolute resistance between the BoL and 100 cycles. This behavior, frequently observed in Si-containing cells, is attributed to particle expansion and mechanical restructuring during early cycling, which can improve interfacial contact and electrochemical reaction kinetics, leading to reduced polarization resistance [46,47]. Given the 10s pulse duration, the DCIR values reflect a combination of ohmic contributions and electrochemical polarization effects, including charge-transfer and SEI resistances, rather than purely electronic resistance. The highest DCIR values were observed for Type 1 Press, while for all other cells the DCIR remained nearly constant between 100 and 300 cycles and increased slightly by the 400th cycle. One of the Type 2 Press cells (marked with *) lacked a proper four-point connection and was therefore excluded from the DCIR analysis. However, this limitation did not affect the capacity measurements. Notably, configurations incorporating foam—Type 1 PCB and the foam-based reference—exhibited nearly identical DCIR trends with slightly reduced resistance growth, indicating that rigid compression has a negative impact on DCIR evolution during cyclic aging. The remaining SoCs (25% and 75%) are shown in **Fig. S7**.

3.4. Pressure homogeneity

Pressure homogeneity within battery cell stacks can be assessed through several established experimental and modeling approaches. Distributed displacement or thickness change measurements, such as laser-based scanning, provide local deformation profiles, where variations across measurement points indicate pressure uniformity [48–50]. Strain gauges mounted at different positions on the cell case or compression fixture similarly reveal spatial differences in local strain [24]. Pressure mapping films (e.g. Fuji Prescale) and tactile sensor arrays (e.g. Tekscan) directly visualize the pressure distribution at the interface between the cell and the compression fixture [10,20,51]. In addition, finite-element simulations (FEM) enable prediction of internal pressure gradients arising from material swelling and boundary conditions, allowing quantitative comparison of local pressure fields [52,53]. Overall, pressure homogeneity is typically expressed using statistical metrics such as standard deviation or spatial uniformity indices derived from experimental or simulated pressure data.

In this work, direct pressure mapping across the entire cell remains challenging for press-based experiments. Three Keyence sensors mounted along the outer edge of the pneumatic press plates provide local displacement readings, which reflect a combination of true stack

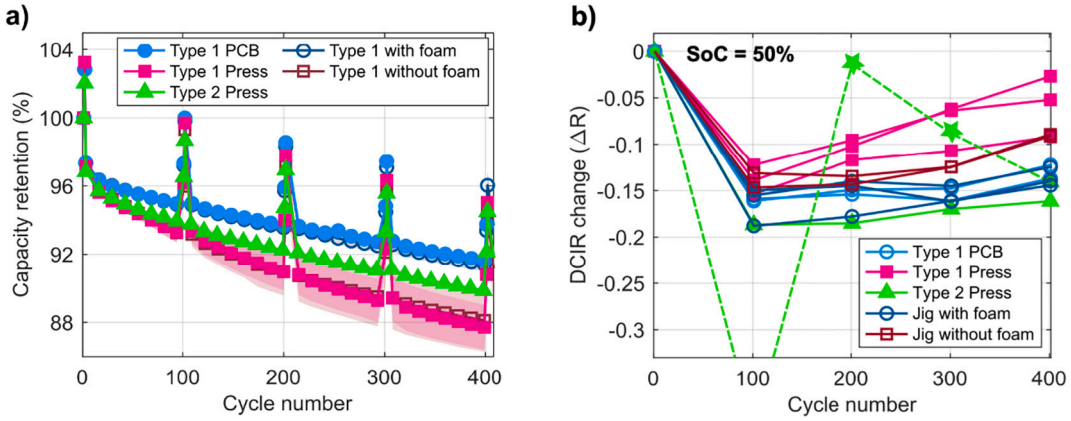

Fig. 8. Electrochemical performance evaluation including: a) Capacity retention results of Type 1 and 2 cells, b) Absolute DCIR change results in PCB and cell press setups and their reference tests (buffered and unbuffered jigs at 50% SoC. Type 2 Press (*) result is an outlier due to the incorrect 4-point cable connection. All measurements were performed at 250 kPa.

expansion and any minor tilting of the press plates. While these measurements enable a qualitative assessment of deformation uniformity, they cannot fully resolve the in-plane pressure distribution. To minimize such artifacts, the press components were carefully aligned with the plate center prior to testing, the sensors were zeroed before each experiment, and the deviations among the three displacement readings remained small (typically below 0.1 μm), indicating good mechanical stability. Fuji Prescale pressure films further confirmed that the applied pressure was uniformly distributed across the plate area.

For the PCB setups, the pressure distribution across the four sensors during cycling was quantified using a misalignment parameter (α). α is defined as the standard deviation of the four sensor readings, normalized to their mean thickness change at the beginning of cycling. It represents the degree of local pressure inhomogeneity within the cell stack. **Fig. S5 (b)** presents the evolution of α over cycling for four cells investigated in the PCB setup. During the initial cycles, α increases, reflecting the development of uneven local pressure distribution as the stack undergoes mechanical settling. Over extended cycling, α stabilizes until the RPT cycles (every 100 cycles), where it decreases and subsequently increases again after the onset of progressive 1C—1C cycling. Between RPT intervals, the α values remain relatively constant, suggesting that the stack reaches a mechanically stable state with no substantial further evolution in local pressure asymmetry. A comparison among cells shows that Cell 1 exhibits the lowest α values throughout cycling and simultaneously the highest capacity retention. In contrast, Cell 4 displays the largest α values and the lowest capacity retention, while Cells 2 and 3 show intermediate behavior. After approximately 200 cycles, α increases for Cell 3, which, however, does not coincide with a deterioration in electrochemical performance. Therefore, a direct correlation between α and capacity retention cannot be fully established based on the available data.

The final experimental results present the pressure distribution using Fuji pressure sensitive films between the cycled cell and the mechanical fixture in both setups, as shown in **Fig. S8 (a)-(c)**. A clear distinction in pressure homogeneity across the cell surface was observed between the three configurations. In the foam-containing setup (left), the Fuji films revealed a highly uniform pressure distribution, indicating consistent contact across the entire cell area. On the other hand, the setups employing rigid plates for Type 1 (middle) and Type 2 cells (right) exhibited noticeable pressure inhomogeneities. Prior to the experiments, the plates had been polished and free of visible surface damage and contamination. Nonetheless, their rigid surface and localized inhomogeneities suggest uneven mechanical loading during compression. A nonuniform pressure distribution on the cell leads to uneven lithium distribution and a possibility of various degradation mechanisms during operation.

Additional post-mortem analyses were conducted to further support the discussion on the electrochemical performance differences between press- and PCB-based setups. Top-view images taken after disassembly of the cells at the fully charged state revealed distinct morphological features of the anodes between the configurations. On the other hand, the cathodes did not display any signs of degradation, and their mechanical integrity was intact. The anodes in both Type 1 and Type 2 Press cells exhibited clear evidence of lithium plating and localized mechanical damage. Type 1 Press cells showed widespread electrode delamination across much of the anode surface, while Type 2 Press cells displayed damage that was more concentrated toward the cell corners. In contrast, the Type 1 PCB cells exhibited a uniform lithiation pattern, intact electrode surfaces and no visible lithium plating, indicating improved interfacial contact and mechanical stability. These observations correlate well with the enhanced capacity retention recorded for the PCB configuration. The presence of lithium plating in the press-cycled cells was further confirmed by isopropanol testing, which produced small gas bubbles upon contact with plated lithium [54]. The corresponding top-view images are provided in **Fig. S9 (a) – (c).**

To gain a deeper understanding of the morphological and structural changes occurring during cycling, SEM analysis was performed on the cathode and anodes cycled in PCB setup before and after 408 cycles in the delithiated state. Both anode center and edge regions were investigated to assess particle morphology, electrode uniformity, and surface integrity. Cross-sectional and top-view images of the anode are shown in **Fig. S6 (a)–(b)**. The uncycled electrode was analyzed before removing the back side of the anode coating, therefore the SEM images show a double-sided coating. The SEM analysis revealed no significant changes in particle morphology, particle cracking or delamination from the current collector for both anode and cathode. The anode electrode thickness increased due to particle expansion upon cycling, resulting in a less dense electrode structure. A thin grey layer surrounding the irregularly shaped, brighter Si particles indicates the formation of the SEI layer, observed both at the electrode center and overhang areas.

Beyond these qualitative differences, several plausible mechanical and electrochemical mechanisms can explain the reduced expansion and breathing amplitude observed in Type 1 Press cells at later cycling stages. In addition to capacity fading, local pressure concentration at electrode edges and corners together with localized lithium plating, irreversible densification of the porous electrodes under prolonged compression, loss of elastic recovery in the separator and current collectors or modified SEI growth under non-uniform pressure are likely contributing factors. Although the present data does not allow us to definitively isolate which mechanism dominates, the combination of post-mortem observations and electrochemical performance suggests that the apparent reduction in expansion amplitude in Type 1 Press cells arises from intertwined mechanical effects, particularly electrode damage and nonuniform pressure distribution, rather than purely electrochemical degradation. These interpretations are consistent with previously reported findings, and they highlight the need for future studies that combine localized pressure mapping with systematic post-mortem analyses to more precisely resolve the interplay between mechanical deformation and electrochemical degradation in compressed cells.

4. Conclusions

This study compares the swelling behavior in lithium-ion pouch cells with a significant share of silicon as active anode material under varying mechanical boundary conditions (constant force and quasi-constant force) using two different measurement approaches: state-of-the-art pneumatic press and a PCB-based system. Through rigorous calibration, fitting and experimental validation, the PCB setup was shown to be a robust and complementary method for determining thickness changes in small-format pouch cells under standard pressure conditions of 250 kPa. Notably, the PCB-based system delivered swelling behavior including maximum and minimum of dilation hysteresis, SoC breathing, and dilation shapes that were in excellent agreement with those obtained using pneumatic presses. In addition, the results of cell thickness growth were also shown to be consistent across different cell formats and at different C-rates. In summary, the suitability of the PCB method was confirmed via a detailed swelling analysis in Si/C-containing cells, demonstrating accurate, scalable, and affordable assessment of the fundamental cell mechanics under quasi-constant pressure. This provides a practical pathway for implementing cost-efficient swelling monitoring in early cell development and diagnostic workflows.

Another objective of this work was to quantify the effect of the buffered and rigid plates on the electrochemical performance. It was shown convincingly that the use of compression foams not only improved the pressure distribution but also positively influenced the capacity retention. Cells operated with compression foams exhibited higher capacity retention, reduced DCIR growth, and less pronounced capacity fade after ~408 cycles. In contrast, rigid plates introduced pressure inhomogeneities that led to localized mechanical damage and correlated electrochemical degradation, as confirmed by post-mortem inspection. The improved contact uniformity in the foam-based setups

was further supported by pressure-sensitive Fuji films and SEM analysis, which verified a more homogeneous surface pressure distribution. These benefits are expected to be particularly relevant for cells with Si-based anodes, given their larger volume changes compared to graphite-only systems.

External swelling measurements were further validated through direct electrode thickness measurements after 408 cycles using a high-precision Mitutoyo micrometer. The measured changes per unit stack were in close agreement with PCB-derived swelling values, showing deviations below 3% for both lithiated and delithiated electrodes. Complementary SEM cross-sections of fully delithiated cells provided in-situ thickness results, with differences between internal and external measurements remaining around 12%. This discrepancy is attributed primarily to the absence of external pressure during SEM imaging and the intrinsic limitations of localized, two-dimensional SEM-based thickness estimation. Together, these findings confirm the reliability of PCB-based swelling measurements.

Mechanical characterization remains essential during both pre-development and series development stages, as it ensures a safe, reliable, and consistent battery performance under realistic operating conditions. For module design in particular, the properties of compression pads and their ability to maintain stable and uniform pressure over time play a critical functional role. Future work will aim to clarify the mechanisms underlying the reduced performance observed in unbuffered cell setups by combining localized pressure mapping with systematic post-mortem analyses. Additional studies will investigate larger cell formats, a broader range of applied pressures, and higher Si contents to further elucidate the mechanical behavior and operational relevance of compression pads in advanced lithium-ion battery systems.

CRediT authorship contribution statement

Magdalena Karolina Zywolko: Writing – original draft, Project administration, Methodology, Investigation, Data curation, Conceptualization. **Andrew Paolo Cádiz:** Writing – review & editing, Supervision, Project administration, Methodology, Conceptualization. **Felix Brauchle:** Supervision, Project administration, Conceptualization. **Sascha Berg:** Writing – review & editing, Validation. **Egbert Figgemeier:** Supervision, Resources.

Declaration of Generative AI and AI-assisted technologies in the writing process

During the preparation of this work the author(s) used ChatGPT to improve the readability and language of the manuscript. After using this tool/service, the author(s) reviewed and edited the content as needed and take(s) full responsibility for the content of the published article.

Declaration of competing interest

The authors declare that they have no known competing financial interests or personal relationships that could have appeared to influence the work reported in this paper.

Acknowledgements

We would like to thank BSBM (*BASF Shanshan Battery Materials*) for the development of high-performance cathode active material used in this study.

Appendix A. Supplementary data

Supplementary data to this article can be found online at https://doi.org/10.1016/j.est.2026.121124.

Data availability

Data will be made available on request.

References

[1] M. Frey, F. Nietfeld, U. Keller, Cell chemistry development for traction batteries at Mercedes-Benz, MTZ worldwide 85 (7–8) (2024) 42–47, https://doi.org/10.1007/s38313-024-1942-0.
[2] L. Mai, et al., A high-resolution dataset on electric passenger vehicle characteristics in China and the European Union, Sci. Data 12 (1) (2025), https://doi.org/10.1038/s41597-025-05770-7.
[3] J. Amici, et al., A roadmap for transforming research to invent the batteries of the future designed within the European large scale research initiative BATTERY 2030 +, Adv. Energy Mater. 12 (17) (2022) https://doi.org/10.1002/aenm.202102785.
[4] O. von Kessel, A. Avdyli, D. Vrankovic, K.P. Birke, Swelling, pressure evolution and aging in high-silicon/graphite composite lithium-ion batteries, J. Power Sources 610 (2024) 234582, https://doi.org/10.1016/j.jpowsour.2024.234582.
[5] T. Deich, M. Storch, K. Steiner, A. Bund, Effects of module stiffness and initial compression on lithium-ion cell aging, J. Power Sources 506 (2021) 230163, https://doi.org/10.1016/j.jpowsour.2021.230163.
[6] S. Hahn, S. Theil, J. Kroggel, K.P. Birke, Pressure prediction modeling and validation for Lithium-ion pouch cells in buffered module assemblies, J. Energy Storage 40 (2021) 102517, https://doi.org/10.1016/j.est.2021.102517.
[7] T. Schabenberger, S. Kücher, A. Durdel, A. Jossen, Influence of pressure peaks occurring during battery module production on performance, J. Energy Storage 122 (2025) 116581, https://doi.org/10.1016/j.est.2025.116581.
[8] T. Deich, S.L. Hahn, S. Both, K.P. Birke, A. Bund, Validation of an actively-controlled pneumatic press to simulate automotive module stiffness for mechanically representative lithium-ion cell aging, J. Energy Storage 28 (2020) 101192, https://doi.org/10.1016/j.est.2020.101192.
[9] P. Li, H. Kim, S.-T. Myung, Y.-K. Sun, Diverting exploration of silicon anode into practical way: A review focused on silicon-graphite composite for Lithium ion batteries, Energy Storage Mater. 35 (2021) 550–576, https://doi.org/10.1016/j.ensm.2020.11.028.
[10] V. Müller, et al., Journal of the electrochemical society effects of mechanical compression on the aging and the expansion behavior of Si/C-composite|NMC811 in different Lithium-ion battery cell formats, J. Electrochem. Soc. 166 (15) (2019), https://doi.org/10.1149/2.1121915jes].
[11] J. Cui, et al., Effect of continuous pressures on electrochemical performance of Si anodes, Mater. Today Energy 20 (2021) 100632, https://doi.org/10.1016/j.mtener.2020.100632.
[12] Otto von Kessel, T. Hoehl, P. Heugel, F. Brauchle, Dragoljub Vrankovic, Kai Peter Birke, Electrochemical-mechanical parameterization and modeling of expansion, pressure, and porosity evolution in NMC811|SiOx-graphite lithium-ion cells, J. Electrochem. Soc. 170 (9) (2023) 090534, https://doi.org/10.1149/1945-7111/ace1aa.
[13] A.J. Louli, J. Li, S. Trussler, C.J. Fell, J.R. Dahn, Volume, pressure and thickness evolution of Li-ion pouch cells with silicon-composite negative electrodes, J. Electrochem. Soc. 164 (12) (2017) A2689–A2696, https://doi.org/10.1149/2.1691712jes.
[14] K. Bischof, Marius Flügel, M. Hölzle, M. Wohlfahrt-Mehrens, T. Waldmann, Aging mechanism for calendar aging of Li-ion cells with Si/graphite anodes, J. Electrochem. Soc. 171 (1) (2024) 010510, https://doi.org/10.1149/1945-7111/ad1b7c.
[15] P. Kargl, et al., Investigation of voltage and expansion hysteresis of Si-alloy-C/NMC622 pouch cells using dilatometry, J. Power Sources 548 (2022) 232042, https://doi.org/10.1016/j.jpowsour.2022.232042.
[16] G.G. Eshetu, et al., Production of high-energy Li-ion batteries comprising silicon-containing anodes and insertion-type cathodes, Nat. Commun. 12 (1) (2021), https://doi.org/10.1038/s41467-021-25334-8.
[17] J. Cannarella, C.B. Arnold, State of health and charge measurements in lithium-ion batteries using mechanical stress, J. Power Sources 269 (2014) 7–14, https://doi.org/10.1016/j.jpowsour.2014.07.003.
[18] A. Aufschläger, A. Durdel, L. Kraft, A. Jossen, Optimizing mechanical compression for cycle life and irreversible swelling of high energy and high power lithium-ion pouch cells, J. Energy Storage 76 (2024) 109883, https://doi.org/10.1016/j.est.2023.109883.
[19] J. Cannarella, C.B. Arnold, Stress evolution and capacity fade in constrained lithium-ion pouch cells, J. Power Sources 245 (2014) 745–751, https://doi.org/10.1016/j.jpowsour.2013.06.165.
[20] A. Barai, et al., The effect of external compressive loads on the cycle lifetime of lithium-ion pouch cells, J. Energy Storage 13 (2017) 211–219, https://doi.org/10.1016/j.est.2017.07.021.
[21] A. Aufschläger, S. Kücher, L. Kraft, F. Spingler, P. Niehoff, A. Jossen, High precision measurement of reversible swelling and electrochemical performance of flexibly compressed 5 ah NMC622/graphite lithium-ion pouch cells, J. Energy Storage 59 (2023) 106483, https://doi.org/10.1016/j.est.2022.106483.
[22] E. Michelini, P. Höschele, S.F. Heindl, S. Erker, C. Ellersdorfer, Experimental investigation on reversible swelling mechanisms of Lithium-ion batteries under a varying preload force, Batteries 9 (4) (2023) 218, https://doi.org/10.3390/batteries9040218.
[23] P. Heugel, Wolfgang Märkle, T. Deich, O. von Kessel, Jens Tübke, Thickness change and jelly roll deformation and its impact on the aging and lifetime of commercial

18650 cylindrical Li-ion cells with silicon containing anodes and nickel-rich cathodes, J. Energy Storage 53 (2022) 105101, https://doi.org/10.1016/j.est.2022.105101.
[24] L. Willenberg, et al., The development of jelly roll deformation in 18650 lithium-ion batteries at low state of charge, J. Electrochem. Soc. 167 (12) (2020) 120502, https://doi.org/10.1149/1945-7111/aba96d.
[25] L.K. Willenberg, P. Dechent, G. Fuchs, D.U. Sauer, E. Figgemeier, High-precision monitoring of volume change of commercial Lithium-ion batteries by using strain gauges, Sustainability 12 (2) (2020) 557, https://doi.org/10.3390/su12020557.
[26] L.D. Sutter, Gert Berckmans, M. Marinaro, M. Wohlfahrt-Mehrens, Maitane Berecibar, Joeri Van Mierlo, Mechanical behavior of silicon-graphite pouch cells under external compressive load: Implications and opportunities for battery pack design, J. Power Sources 451 (2020) 227774, https://doi.org/10.1016/j.jpowsour.2020.227774.
[27] C. Yang, N. Sunderlin, W. Wang, C.W. Churchill, M. Keyser, Compressible battery foams to prevent cascading thermal runaway in Li-ion pouch batteries, J. Power Sources 541 (2022) 231666, https://doi.org/10.1016/j.jpowsour.2022.231666.
[28] M. Wünsch, J. Kaufman, D.U. Sauer, Investigation of the influence of different bracing of automotive pouch cells on cyclic liefetime and impedance spectra, J. Energy Storage 21 (2018) 149–155, https://doi.org/10.1016/j.est.2018.11.019.
[29] Hendrik Laufen, et al., Correlation between voltage, strain, and impedance as a function of pressure of a nickel-rich NMC lithium-ion pouch cell, Adv. Mater. Technol. 9 (8) (2024), https://doi.org/10.1002/admt.202301965.
[30] D. Sauerteig, S. Ivanov, H. Reinshagen, A. Bund, Reversible and irreversible dilation of lithium-ion battery electrodes investigated by in-situ dilatometry, J. Power Sources 342 (2017) 939–946, https://doi.org/10.1016/j.jpowsour.2016.12.121.
[31] P. Daubinger, F. Ebert, S. Hartmann, G.A. Giffin, Impact of electrochemical and mechanical interactions on lithium-ion battery performance investigated by operando dilatometry, J. Power Sources 488 (2021) 229457, https://doi.org/10.1016/j.jpowsour.2021.229457.
[32] F. Brauchle, F. Grimsmann, K.P. Birke, New Eddy-current sensor setup for high-resolution Lithium-ion cell dilation measurements, IEEE Sensors J. 23 (15) (2023) 17002–17010, https://doi.org/10.1109/jsen.2023.3290349.
[33] F. Brauchle, F. Grimsmann, K.P. Birke, Spatially resolved degradation and inhomogeneity analysis of lithium-ion pouch cells using an array of eddy-current sensors, J. Energy Storage 83 (2024) 110740, https://doi.org/10.1016/j.est.2024.110740.
[34] C. Briody, B. Duignan, S. Jerrams, S. Ronan, Prediction of compressive creep behaviour in flexible polyurethane foam over long time scales and at elevated temperatures, Polym. Test. 31 (8) (2012) 1019–1025, https://doi.org/10.1016/j.polymertesting.2012.07.006.
[35] M. Göttlinger, P. Daubinger, W. Stracke, S. Hartmann, G.A. Giffin, Influence of external pressure on silicon electrodes in lithium-ion cells, Electrochim. Acta 419 (2022) 140354, https://doi.org/10.1016/j.electacta.2022.140354.
[36] I.R. Henriques, L. Rouleau, D.A. Castello, L.A. Borges, J.-F. Deü, Viscoelastic behavior of polymeric foams: Experiments and modeling, Mech. Mater. 148 (2020) 103506, https://doi.org/10.1016/j.mechmat.2020.103506.
[37] C.V. Valivarthy, J.P. Youngblood, D.S.M. Varma, J. Vishnu, K.V.M. Kumar, M. R. Chandan, Visco-hyperelastic modeling of auxetic polyurethane foams, Polym. Bull. 82 (11) (2025) 5833–5852, https://doi.org/10.1007/s00289-025-05768-6.
[38] J. Deng, et al., A comprehensive method with verification for characterizing the visco-hyperelastic material model of polyurethane foam of passenger car seats, Materials 18 (15) (2025) 3526, https://doi.org/10.3390/ma18153526.
[39] Katleen van Nuffel, Optimizing Lithium-ion battery longevity with foam compression pads, ATZelectronics worldwide 20 (7–8) (2025) 58–63, https://doi.org/10.1007/s38314-025-2030-1.
[40] T. Boivin, B. Mathieu, W. Porcher, O. Gillia, Breathing of a silicon-based anode: Mechanical discrete approach using DEM, J. Electrochem. Soc. 171 (1) (2024) 010505, https://doi.org/10.1149/1945-7111/ad14cf.
[41] D. Vidal, S. Genies, E. De Vito, M. Tulodziecki, W. Porcher, Operando swelling measurement of silicon carbon composite based anode in pouch cell: Effect of external pressure, balancing and anode initial porosity, J. Energy Storage 64 (2023) 107174, https://doi.org/10.1016/j.est.2023.107174.
[42] K. Chen, et al., Degradation mechanism and assessment for different cathode based commercial pouch cells under different pressure boundary conditions, Energy Storage Mater. 73 (2024) 103793, https://doi.org/10.1016/j.ensm.2024.103793.
[43] G. Bridgewater, M.J. Capener, J. Brandon, M.J. Lain, M. Copley, E. Kendrick, A comparison of Lithium-ion cell performance across three different cell formats, Batteries 7 (2) (2021) 38, https://doi.org/10.3390/batteries7020038.
[44] D. Beck, P. Dechent, M. Junker, D.U. Sauer, M. Dubarry, Inhomogeneities and cell-to-cell variations in Lithium-ion batteries, a review, Energies 14 (11) (2021) 3276, https://doi.org/10.3390/en14113276.
[45] J. Lin, H.N. Chu, C.W. Monroe, D.A. Howey, Anisotropic thermal characterisation of large-format lithium-ion pouch cells, Batteries Supercaps 5 (5) (2022), https://doi.org/10.1002/batt.202100401.
[46] G.F.I. Toki, M.K. Hossain, W.U. Rehman, R.Z.A. Manj, L. Wang, J. Yang, Recent progress and challenges in silicon-based anode materials for lithium-ion batteries, Industrial Chemistry & Materials (2023), https://doi.org/10.1039/D3IM00115F.
[47] T. Sours, et al., Early-cycle current pulses enable ML-based battery cycle life predictions across manufacturers, arXiv preprint arXiv (2024), 2410.05326v2, Available: https://arxiv.org/abs/2410.05326v2.
[48] B. Rieger, et al., Multi-directional laser scanning as innovative method to detect local cell damage during fast charging of lithium-ion cells, J. Energy Storage 8 (2016) 1–5, https://doi.org/10.1016/j.est.2016.09.002.
[49] J. Sturm, F.B. Spingler, B. Rieger, A. Rheinfeld, A. Jossen, Non-destructive detection of local aging in Lithium-ion pouch cells by multi-directional laser scanning, J. Electrochem. Soc. 164 (7) (2017) A1342–A1351, https://doi.org/10.1149/2.0161707jes.
[50] D. Clerici, F. Mocera, A. Somà, Experimental characterization of Lithium-ion cell strain using laser sensors, Energies 14 (19) (2021) 6281, https://doi.org/10.3390/en14196281.
[51] S. Friedrich, S. Helmer, L. Reuter, J.L.S. Dickmanns, A. Durdel, A. Jossen, Effect of mechanical pressure on rate capability, lifetime, and expansion in multilayer pouch cells with silicon-dominant anodes, J. Electrochem. Soc. 171 (9) (2024) 090503, https://doi.org/10.1149/1945-7111/ad71f6.
[52] P. Gupta, P. Gudmundson, Modeling of local electrode stresses and pressures in lithium-ion battery packs using three-dimensional homogenization, J. Power Sources 582 (2023) 233514, https://doi.org/10.1016/j.jpowsour.2023.233514.
[53] H.-Y. Jeong, J. Park, Development of a homogenized finite element model for pouch Lithium-ion battery cells considering porosity and pressure sensitivity, Energies 17 (5) (2024) 1162, https://doi.org/10.3390/en17051162.
[54] M. Grünebaum, A. Buchheit, C. Lürenbaum, M. Winter, H.-D. Wiemhöfer, Ester-based battery solvents in contact with metallic Lithium: Effect of water and alcohol impurities, J. Phys. Chem. C 123 (12) (2019) 7033–7044, https://doi.org/10.1021/acs.jpcc.9b00331.